THERMAL INFLUENCE OF WELDING PROCESS ON STRENGTH OVERMATCHING OF THIN DISSIMILAR SHEETS JOINTS

M. Iordachescu[1], J. Ruiz-Hervias[1], D. Iordachescu[2], A. Valiente[1], L. Caballero[1]

[1]Materials Science Department, E.T.S. de Ingenieros de Caminos, Canales y Puertos, Universidad Politécnica de Madrid, C/Professor Aranguren s/n, 28040 Madrid, España
E-mail: miordachescu@mater.upm.es

[2]Centro Láser-UPM, Universidad Politécnica de Madrid
Campus Sur U.P.M. (Edificio "La Arboleda"), Ctra. De Valencia, km 7,3, 28031 Madrid, Spain
E-mail: danut.iordachescu@upm.es

ABSTRACT

The investigation addresses the overall performance of black and white joints (BWJ) of low carbon steel and stainless steel thin sheets achieved by laser hybrid welding. First, thermal field modelling is carried out by considering Goldak's double ellipsoidal heat source model, together with a contribution of the authors related to the shape coefficients. In parallel, the technological development of BWJ laser hybrid welding is also addressed. Material characterisation by means of macro and microstructural examination and hardness tests is performed. The overall tensile performance of BWJ is discussed together with the weld metal strength overmatching. The tensile tests results indicate that in case of transversally loaded joints, the positive difference in yield between the weld metal and the base materials protects the weld metal from being plastically deformed; the flat transverse tensile specimens loading up to failure reveals large strains in low carbon steel, far away from the weld.

KEY WORDS: Black & White Joint, laser hybrid welding, overmatching joint, hardness, tensile test.

1. INTRODUCTION

The most common issue in dissimilar metals welding (DMW) is due to the differences in the physical properties (mainly the coefficient of thermal expansion and heat conductivity) of the base metals, as well as on certain level of metallurgical incompatibility. The weld thermal cycle produces differently featured heat affected zone (HAZ), accompanied by microstructural changes in the engineered microstructure, which may lead to an important loss of joint quality. Despite several reported weld-related failures, DMW is often used in chemical and petrochemical industry (reactors, tubes and pipelines), and in power generation, including nuclear plants (nuclear steam generator channel heads, pressurized water reactors, tube sheets and reheat piping).

Such joints may involve the combination of low carbon steel (white ferrite) and stainless steel (black austenite) known as "black and white joints" (BWJ) [1]. First, research was focused on the temperature influence on BWJ of thin sheets. This is emerging nowadays due to cost saving and satisfactory service performance. Results of this theoretical approach were used to develop Laser-GMA hybrid welding (LHW) for achieving BWJ. This process combines the advantages of both laser and GMA welding, namely fast welding speed, low heat input, small HAZ and large weld aspect ratio (depth to width) [2]. Substantial differences in strength properties of the base metals and of the fusion zone (FZ) of the LH joints inevitably occur due to the high thermal gradients characterising this welding process. This might be explained by the carbon diffusion and formation of harmful constituents [3].

An adequate LHW technology development was based on the thermal field modelling; the temperature influence on the metals dilution and a suitable filler metal selection was addressed using Schaeffler Constitution Diagram. In addition, for an in-depth understanding of the processing temperature influence, detailed macro and microstructural examination of the BWJ and related micro-hardness analysis were performed. Finally, the overall tensile performance of BWJ was experimentally assessed, and the weld metal strength overmatching was discussed.

2. THEORETICAL APPROACH

2.1. Thermal simulation

The FE thermal simulation of the dissimilar plates butt welding was carried out using an elliptical disk moving heat source model [4, 5]. Two plates of low carbon steel and stainless steel of equal sizes (200 mm x 300 mm

and 3 mm thickness) were considered. The heat transfer in the plates was modelled as 2D heat transfer problem using SHELL element group type *(Element Group: SHELL 4, Elements: 6240)*. The temperature influence through thickness was neglected; 4-noded quadrilateral elements were used for the plate's discretization together with the mesh refining in the welding area, allowing the accurate prediction of temperature distribution at specific time steps.

Considering a welding efficiency of 70%, the finite element analysis uses the heat input value of 4600 W and the welding speed of 3 m/min. The elliptical disk heat source parameters estimated values were: a = 2.5 mm, c_f = 3 mm, c_r = 9 mm. Consequently, the proportion coefficients for heat apportionment in the front and rear side of the welding pool values were: $f_f = 0.5$ and $f_r = 1.5$.

Table 1. Chemical composition, [%]

	C	Mn	Si	Cr	Cu	Ni	S	P
LCS	0.155	0.6	0.25	0.17	0.04	0.02	0.035	0.029
SS	0.022	1.81	0.41	18.1	0.33	9.2	0.08	0.025

Table 2. Low carbon steel, St37-2 - thermal conductivity λ, mass density ρ, and specific heat capacity c_p

St37-2 Temp. [^{0}C]	λ [W/m $\cdot^0$C]	ρ [kg/m^3]	c_p [J/kg $\cdot^0$C]
20	48.07	7850	465
200	43.89	7770	527
400	38.04	7700	606
500	35.53	7670	685
600	31.77	7630	761
700	29.26	7610	936
800	25.50	7590	685
1000	28.01	7510	618
1300	31.35	7400	644
1600	34.28	7100	840

Table 3. Stainless steel, AISI 304L - thermal conductivity λ, mass density ρ, and specific heat capacity c_p

St37-2 Temp.[^{0}C]	λ [W/m $\cdot^0$C]	ρ [kg/m^3]	c_p [J/kg $\cdot^0$C]
20	15.93	7920	510,7
200	17.21	7840	523,3
400	20.11	7750	540
500	21.74	7710	552,6
600	23.84	7660	569,4
700	25.58	7610	548,4
800	26.74	7560	586,1
1000	28.02	7460	598,7
1300	32.35	7310	611,2
1600	36.37	7210	619,6

The heat source model consider the heat flux losses by convection and radiation; thus, during the FE analysis, a convection heat transfer coefficient of 15 W/m^{2}K, the radiative emissivity of 0.7, and the Stefan-Boltzmann constant of 5.67 x10^{-8} W m^{-2}K^{-4} were used.

The chemical composition of the base metals, low carbon steel (LCS) and stainless steel (SS), is presented in Table 1. Tables 2-3 contain the other materials thermo-physical data used into the finite element analysis [6, 7]. The melting temperature range is $T_{AISI\ 304L}$ = 1400 – 1450^{0}C for stainless steel and $T_{St\ 37\text{-}2}$ = 1430 – 1500^{0}C for the low carbon steel.

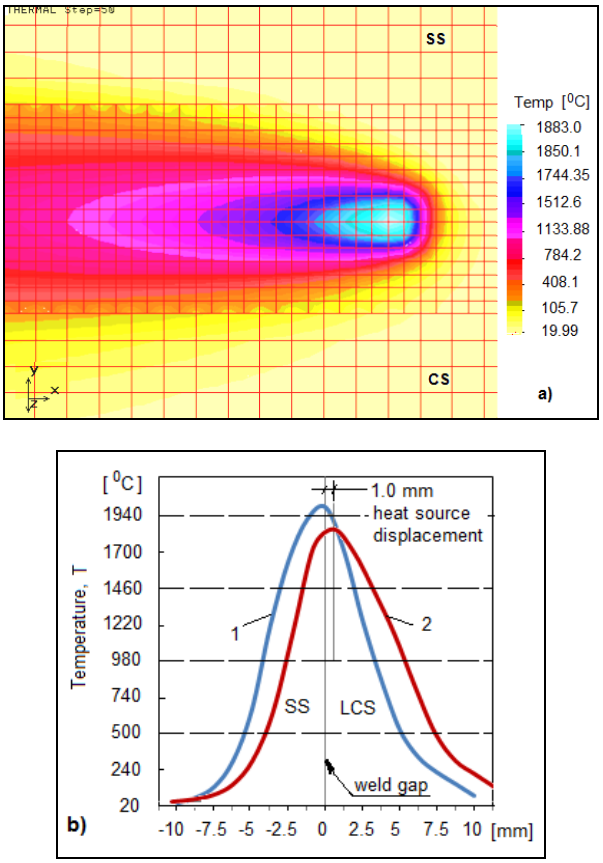

Figure 1. Temperature field on AISI 304L – St 37-2 (SS-LCS) welding: a) The heat source longitudinal axis was displaced 1 mm from the weld gap, on LCS; the welding quasi-stationary phase is corresponding to a weld time of 4s; b) Temperature transverse variation: 1 – the heat source longitudinal axis coincide with the weld gap; 2 – the heat source longitudinal axis is moved on LCS.

Figure 1a illustrates the numerical results of the thermal analysis corresponding to the welding process quasi-stationary phase, captured after a weld time of 4s. It can be noticed an emphatic asymmetry of the temperature field (related to the welding direction), as a result of different thermal properties of the base metals and of the heat source displacement of 1mm on LCS side.

Figure 1b shows the differences on temperature transverse variation in case of 1mm parallel displacement of the heat source from the weld gap; LCS participation at the weld joint formation increases and a

larger HAZ is formed on its side. Moreover, due to the base metals differences in thermal conductivity the process peak temperature decreases as well.

The thermal analysis indicate that the heat source paralel displacement at different distances from the weld gap critically influences the metals participation at the joint formation. This effect, less important in case of similar metal joining, might be very interesting, when a specific microstructure of the weld is requested.

2.2. Temperature distribution and base metals participation at joint formation

Asuming that weld obtaining, without using a filler metal, is influenced by the correspondent heat input on each base material, previous data of the temperature variation on the heat source transversal axis were used to estimate their apportionment at joint formation.

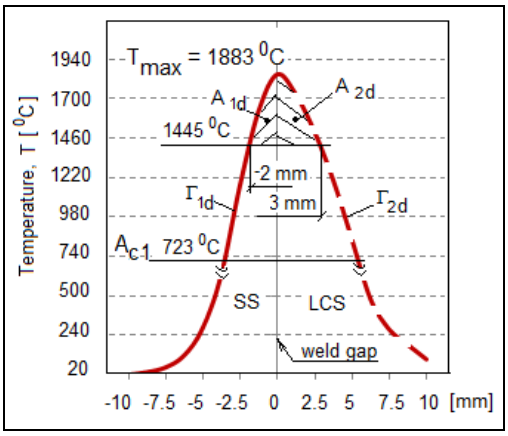

Figure 2. Estimated temperature transverse variation influence on dissimilar metals welding when the heat source longitudinal axis is moved on LCS; A_{1d} - area of heat source influence on SS; A_{2d} - area of heat source influence on LCS; Γ_{1d} – temperature distribution curves on SS; Γ_{2d} – temperature distribution curves on LCS.

As Figure 2 shows, on the temperature transverse variation chart presenting the case of 1mm parallel displacement of the heat source from the weld gap several parameters were defined: Γ_{1d}, temperature transverse variation curve in SS; A_{1d}, corresponding area of heat source influence in SS; Γ_{2d} temperature transverse variation curve in LCS; A_{2d} area of heat source influence in LCS. Previous numerical results of the thermal analysis in the temperature domain [A_{c1}, T_{max}] were considered for Γ curves estimation; the domain restriction, allowing better curves estimation, and errors reduction, respectively. Thus, two polynomial regressions of 3rd order were found:

$$\Gamma_{1d} = f_{SSd}(x) = -12.117\,x^3 - 118.4\,x^2 + 51.733\,x + 1883 \quad (1)$$

$$\Gamma_{2d} = f_{LCSd}(x) = -1.1905x^3 - 15.303x^2 - 94.263x + 1883 \quad (2)$$

The areas of heat source influence were obtained by integrating the above Γ curves, on different x domains corresponding to each fusion zone width:

$$A_{1d} = \left| \int_{-x}^{0} \Gamma_{1d}(x)\,dx \right| \qquad x \in [-2; 0] \quad (3)$$

$$A_{2d} = \int_{0}^{x} \Gamma_{2d}(x)\,dx \qquad x \in [0; 3] \quad (4)$$

Finally, it was assumed that the base metals dilution coefficients, K_1 and K_2 can be computed through the corresponding areas of heat source influence.

$$K_1 = \frac{A_{1d}}{A_{1d} + A_{2d}} \cdot 100\,[\%] \text{ and } K_2 = \frac{A_{2d}}{A_{1d} + A_2 d} \cdot 100\,[\%] \quad (5)$$

The estimated dilution coefficients were 40% for SS and 60% for LCS.

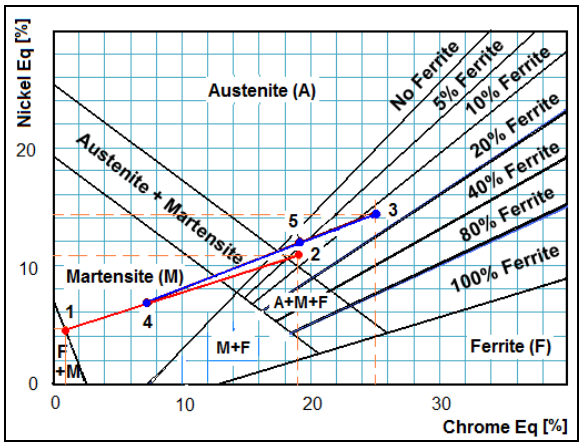

Figure 3. Estimated weld metal structure

The set of dilution coefficients together with the Schaeffler Constitution Diagram [8, 9] for stainless steel weld metal were further used for and adequate selection of the filler metal. Although nowadays WRC-1992 diagram is more accurate in predicting the ferrite content for many weld metals, Kou [8] has shown that Schaeffler Constitution Diagram is reasonable accurate for predicting the type of the weld metal constituents in case of dissimilar metal joining. In this diagram, Nickel and other elements that form austenite are plotted against Crome and other elements that form ferrite, using the following formula:

$$Ni_{eq} = \%Ni + 30\%C + 0.5\%Mn \quad (6)$$

$$Cr_{eq} = \%Cr + Mo + 1.5\%Si + 0.5\%Nb \quad (7)$$

Thus, for St 37-2: Ni_{eq} = 4.972 and Cr_{eq} = 0.785, and for AISI 304 L: Ni_{eq} = 10.765 and Cr_{eq} = 18.715 (points 1 and 2 in Figure 3).

As shown in Figure 3, on the dilution line which couples the LCS point 1, and the SS point 2, is plotted the point 4, which estimates the weld metal constituents in case of 40% SS and 60% LCS dilution, previously found (eq. 5). The point indicates that without using a filler metal, the weld metal solidification, will be situated into the martensite region of the Schaeffler Diagram. This problem can be overcome if a higher alloyed austenitic filler metal is used.

Therefore, INTERFIL 309LSi filler wire was selected for future testing of the LHW process. The wire Ni_{eq} = 14.24 and Cr_{eq} = 22.35 couple calculus considers the chemical composition presented in Table 4.

Table 4. INTERFIL 309LSi filler metal chemical composition, [%]

C	Mn	Si	Cr	Cu	Mo	Ni	S	P	N
0.5	1.98	0.7	18.5	0.3	2.5	12.5	0.015	0.02	0.06

After plotting the wire representative point 3 and assuming the dissimilar base metals dilution of 30%, on the dilution line which couples the points 4 - 3, is plotted the point 5, which estimates the weld metal microstructure. It results that the predicted weld microstructure is a mixture of austenite with a small amount of ferrite, of about 5%. According to Berretta et al. [2] the Cr and Ni equivalent values of the point 5 are located in a region of the Schaeffler Diagram with less probability of defects formation in the weld. Lancaster [9] showed that a ±4% error might occur in the area of low ferrite content from the Schaeffler Diagram, which might produce the 5 point falling into the A+M+F domain.

3. EXPERIMENTAL RESULTS

3.1. Experimental procedure

The results from these theoretical approaches were applied for Laser-GMA hybrid single pass butt welding of low carbon steel, St 37, and stainless steel, AISI 304 L, plates (200 mm x 300 mm) of 3 mm thickness; INTERFIL 309LSi filler wire (1.2 mm diameter) and ARCAL*12 shielding gas were used. The Nd:YAG laser DY 033 (3300 W) focal point position relative to the upper side of the plates was -1 mm for the laser welding speed of 3 m/min. The GMAW source (Trans Puls Synergic 5000) parameters were: arc voltage, V= 23 V, welding current intensity, I = 230 A and wire feeding speed, v_w= 8 m/min.

The experiments involved the heating sources moving on LCS side, reproducing the thermal analysis case.

Standard procedures were used to prepare the metallographic and tensile specimens. Macro and microstructures of processed materials were analyzed by optical microscopy after previous polishing and etching with Kalling no. 2 reagent. The bead shape measurements were made using an optical perfilometer with an image analysis system. Vickers HV1 hardness measurements were made according to UNE EN ISO 6507. Tensile features of the base materials and of the welded joint were evaluated following the ASTM E-8M procedure.

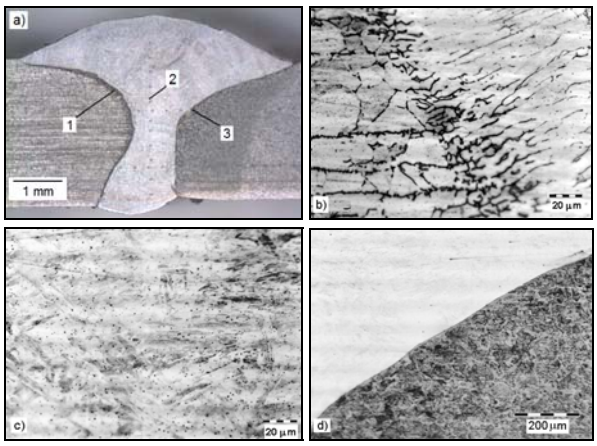

Figure 4. LHW of LCS-SS thin sheets: a) weld cross-section macrostructure; b) optical microstructure of the HAZ in SS and weld FZ; c) weld microstructure; d) optical microstructure of the FZ and HAZ in LCS.

3.2. Macro and microstructure features

The macrostructure of the LH weld cross-section is presented in Figure 4a; the geometry of the single pass LH weld being a combination of the appearance of laser and arc weld beads. The fusion zone shape, showing higher dilution of SS at the weld root is due to the metals differences in thermal conductivity (SS smaller conductivity comparing with the LCS) and heat reflexion on thin plates bottom side. LCS higher conductivity also explains the larger HAZ formation on its side, well illustrated by the weld cross-section macrostructure.

LH dissimilar joint features are presented in Figure 4b-d. Stainless steel HAZ (Figure 4b) shows the gradual transition from coarsed grains of austenite and vermicular ferrite dentrites up to the weld fusion line characterized by lacy ferrite.

Figure 4c illustrates the main weld bead microstructure as consisting essentially of martensite, as a consequence of increased carbon diffusion from LCS into the weld, dispersed δ-ferrite and small amounts of austenite. Due to increased dilution of LCS and laser processing welding speed, close to the SS fusion line (Figure 4b), the weld metal is formed by solidified fine columnar austenite between δ-ferrite epitaxial grown grains. Relatively good agreement was encountered between the weld microstructure experimentally found and the analytically predicted one; thus, compared with the

experiments, a 4% error on 7 point location in Figure 3, being obtained by evaluating the weld microstructure through the base metals dilution and Schaeffler diagram.

At the weld interface on the ferritic side, a darkly etched area with an adjacent decarburized narrow band was found (Figure 4d). St 37-2 carbon steel HAZ illustrate the transition from the grain coarsed microstructure region of Widmanstatten ferrite, bainite and acicular ferrite which follows the weld bead solidification front, up to the grain refined region.

Recent investigation of Shirzadi et al., [10], has shown that the martensite formation into the stainless steels weld bead might be capable of reducing the distortion of the weld. Therefore, the resulted weld microstructure obtained by moving the heat source longitudinal axis on LCS is beneficial for dissimilar thin sheets LH welds producing.

3.2. Joint mechanical characteristics

Several mechanical properties were used to characterize the dissimilar LH welds between LCS-SS. The goal was to ensure that the produced dissimilar LH weld is not the weakest component of a structure. In this view, pertinent mechanical tests as microhardness, and tensile tests were made.

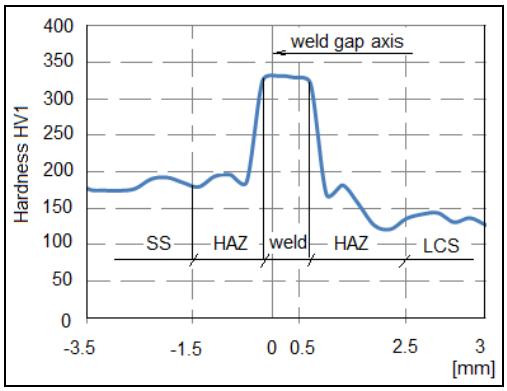

Figure 5. Microhardness profile on LHW dissimilar joint

The weld transversal hardness field features are presented in Figure 5. The microhardness of the weld bead is greater than of both AISI 304L and St 37-2 base materials; its overall average of 330 HV1 being characteristic of a combined austenitic-martensitic-ferritic structure, as the weld microscopy revealed and Missori, [11], previously reported.

The microhardness of the weld HAZs interface on both sides is less than that measured in the weld bead, but is higher than that found in the correspondent base metals. A peak value of 193 HV1 was found in the SS HAZ, on grown vermicular ferrite dentrites. Hardness measurements on the coarse grain microstructure of LCS HAZ showed maximum values of 156 HV1; this maximum hardness value found in the LCS HAZ is comparable with the stainless steel hardness mean value of 160 HV1.

The resulted hardness profiles suggest that the weld overmatch in strength both base metals, recommending the laser-GMA hybrid welding variant, by using the heat source displacement on LCS part, for future usage in dissimilar joints producing.

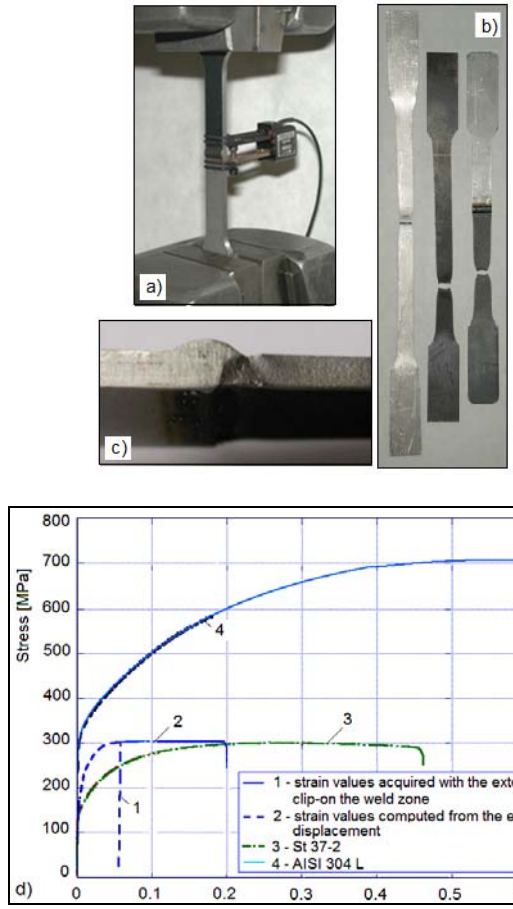

Figure 6. Tensile test results: a) extensometer clip-on position capturing the dissimilar joint; b) Flat transverse tensile specimens machined from the base metals and from the dissimilar joint; c) stiffening effect induced by the weld; c) stress-strain curves obtained by testing transverse tensile specimens of: 1- LH dissimilar (LCS-SS) welds with the extensometer clip-on position capturing weld; 2- LH dissimilar (LCS-SS) welds with strain values were computed from the machine; 3- St 37-2 (LCS) base metal; 4- AISI 304L (SS) base metal.

Transverse tensile tests (Figure 6a,c), in which the loading axis is perpendicular to the weld bead, were performed. The goal was to verify that the overload failure occurs in the lower strength base metal, rather than in the weld metal or HAZ. The test shows (Figure 6b,c) that the material starts to "flow" in the vicinity of the HAZ, in LCS, but the specimen fails far from the weld, in the base material.

Figure 6d show the stress-strain curves obtained from the flat transverse tensile specimens of the LCS-SS dissimilar joint, loaded under displacement control at 1 mm/min. Firstly, the strain values were acquired through an Instrom 2620-602 extensometer capturing both sides of the joint HAZs and the fusion zone. Second, the nominal strain values were computed based on the overall displacement of the machine. Differences on specimen elongation found were due to the weld induced stiffening effect, of different magnitudes, produced by the joint heterogeneities. The joint (FZ and HAZ) nominal strain was 3.33 times smaller than the overall structural strain of 0.2.

Moreover, it was found that the stress-strain curve obtained from the flat transverse tensile specimens of the dissimilar joint lies between those of the similar joints of the constituent steels (Figure 6d). It is clear that these tests, do not give any information on the local mechanical properties of the weld regions, which were impossible to obtain, due to the small plate thickness and weld dimensions.

The investigation proved that LHW can be successfully applied for thin plates dissimilar welding of SS-LCS, even by moving the heat source longitudinal axis on LCS. In this particular case, the weld overmatching in strength both base metals was found from tensile tests, hardness profile and weld regions microstructures.

According to Davis [12], these strength-overmatched welded joints are designed to ensure the safe service of a welded structure by keeping the flaws, in an elastic weld metal, while the base metal starts to yield. Such an approach ensures that a welded structure can sustain local plastic deformation, important when temporary overloading or geometrical changes occur.

4. CONCLUSIONS

Transient thermal histories resulted from the finite element analysis were used to estimate the influence of the heat source displacement on the base metals dilution coefficients. Thus, the base metals dilution ratio was found and used for predicting the type of the weld metal constituents through the Schaeffler Constitution Diagram. A suitable filler metal chemical composition was selected for the experiments.

The results of the theoretical approaches were applied for Laser-GMA hybrid single pass welding of low carbon steel (St 37) and stainless steel (AISI 304) plates of 3 mm thickness. Macro and microstructural analysis revealed from the beginning that sound dissimilar joints were obtained. The presence of hard and brittle constituents as bainite, martensite and δ-ferrite justifies the microhardness increase in the weld region. In addition to the different thermo-physical properties of the base metals, the heat source moving to the higher heat conductive material also explains the different dimensions of the HAZs; a narrower HAZ being found between the stainless steel and the weld.

The tensile tests results indicate that in case of transversally loaded joints, the positive difference in yield between the weld metal and the base materials (overmatching welds) protects the weld metal from being plastically deformed; Tensile tests up to failure revealed large strains in the low carbon steel side, far away from the weld. This is due to the strength overmatch, hardness profile and microstructures developed in the weld regions.

5. REFERENCES

[1] Sun, Z., *Feasibility of producing ferritic/austenitic dissimilar metal joints by high energy density laser beam process.* Int. J. Pres. Ves. & Piping, vol. 68, 1996, pp. 153-160.

[2] Berretta J.R., W. Rosi, M.D.M. Neves, I.A. Alameida, N.D.J. Vieira, *Pulsed Nd:YAG laser welding of AISI 304 to AISI 420 stainless steels,* Opt. Lasers Eng., vol. 45, 2007, pp. 960-966.

[3] Scutelnicu, E., Iordachescu, M., Iordachescu, D. *Structural modifications in the heterogeneous welded joints*, Welding in the World, 2008, vol. 52 (SPEC. ISS.), pp. 185-189.

[4] Goldak, J., Chakravarti, A., Bibby, M., *A new finite element model for welding heat source*. Metall. Trans. B 15B, 1984, pp. 299–305.

[5] Iordachescu, D., Constantin, E., Georgescu, V., Iordachescu, M., *Antigravity arc welding processes and the weld geometry*. The Annals of "Dunarea de Jos" University of Galati, Fascicle XII, Year X-XI, 1999-2000, pp. 15-18

[6] Rempe J.L., Knudson D.L., *High temperature thermal properties for metal used in LWR vessels*, J. Nucl. Mater., vol. 372, 2008, pp. 350-357.

[7] Murugan S., Kumar P.V., Raj B., Bose M.S.C., *Temperature distribution during multipass welding of plates*, Int. J. Pres. Ves. Pip., vol. 75, 1998, pp. 891-905.

[8] Kou, S., *Welding Metallurgy*, 2nd ed., New York: John Wiley & Sons, Inc., 2003.

[9] Lancaster, J. F., *Metallurgy of Welding,* Cambridge: Abington Publishing, 1999.

[10] Shirzadi A.A., Bhadeshia H.K.D. H., Karlson L., Withers P.J., *Stainless steel weld metal designated to mitigate residual stresses*, Sci. Technol. Weld. Join., 2009, vol. 14, no. 6, pp. 559-565.

[11] Missori, S., *Weld metal microstructures on Dissimilar Steels Laser Beam Welded Joints,* Microsc Microanal 11(Suppl 2), 2005, pp. 1838-1839 (DOI: 10.1017/S1431927605500400)

[12] Davis J.R., *Hardfacing, weld cladding, and dissimilar metal joining*, Metals Handbook, 1993, vol. 6, pp. 817-818.